Journal of
BIOPHOTONICS

FULL ARTICLE

Intravascular magnetomotive optical coherence tomography of targeted early-stage atherosclerotic changes in ex vivo hyperlipidemic rabbit aortas

Jongsik Kim[1], Adeel Ahmad[2], Joanne Li[3], Marina Marjanovic[1,3], Eric J. Chaney[1], Kenneth S. Suslick[1,4], and Stephen A. Boppart[*,1,2,3,5]*

[1] Beckman Institute for Advanced Science and Technology, University of Illinois at Urbana-Champaign, 405 North Mathews Avenue, Urbana, IL, 61801, USA

[2] Department of Electrical and Computer Engineering, University of Illinois at Urbana-Champaign, 619 South Wright Street, Champaign, IL, 61820, USA

[3] Department of Bioengineering, University of Illinois at Urbana-Champaign, 1270 Digital Computer Laboratory MC-278, 1304 W. Springfield Avenue, Urbana, IL, 61801, USA

[4] Department of Chemistry, University of Illinois at Urbana-Champaign, 505 South Mathews Avenue, Urbana, IL, 61801, USA
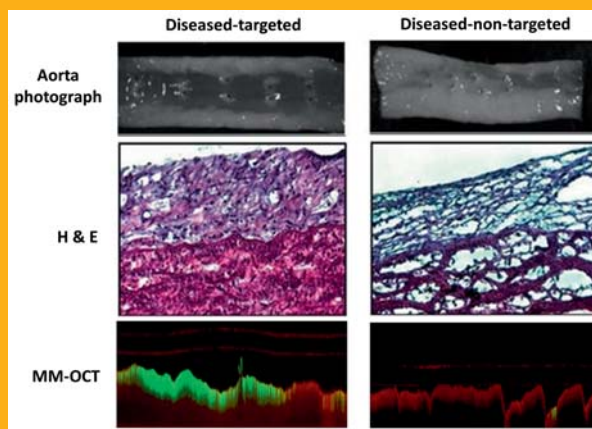
[5] Department of Internal Medicine, University of Illinois at Urbana-Champaign, 190 Medical Sciences Building MC-714, 506 South Mathews Avenue, Urbana, IL, 61801, USA

We report the development of an intravascular magneto-motive optical coherence tomography (IV-MM-OCT) system used with targeted protein microspheres to detect early-stage atherosclerotic fatty streaks/plaques. Magnetic microspheres (MSs) were injected *in vivo* in rabbits, and after 30 minutes of *in vivo* circulation, excised *ex vivo* rabbit aorta samples specimens were then imaged *ex vivo* with our prototype IV-MM-OCT system. The alternating magnetic field gradient was provided by a unique pair of external custom-built electromagnetic coils that modulated the targeted magnetic MSs. The results showed a statistically significant MM-OCT signal from the aorta samples specimens injected with targeted MSs.

Representative magnetomotive signal (green) using targeted and non-targeted magnetomotive microspheres in atherosclerotic diseased rabbit aortas.

* Corresponding author: e-mail: boppart@illinois.edu, Phone: +01 217 333 8598, Fax: +01 217 333 5833

1. Introduction

Atherosclerosis is an arterial vascular disease in which an artery wall thickens and hardens as a result of the accumulation of white blood cells, cholesterol, and calcium. Advanced stages of atherosclerotic lesions can narrow the arterial lumen and restrict oxygen-rich blood flow to tissue, such as the myocardium. Vulnerable plaques, the most threatening form of atherosclerosis, can rupture due to mechanical stress (e.g., pulse pressure), initiating a series of events including blood coagulation, a sudden increase in vascular resistance that can progress to total occlusion of the vessel, and/or emboli (i.e., small blood clots detached from the endothelium) that can shed into peripheral arteries. These cardiovascular events can result in stroke or myocardial infarction, the leading cause of death in the United States [1].

Optical coherence tomography (OCT) is a high-resolution biomedical imaging modality that has become an established standard for clinical ophthalmic imaging [2] and is rapidly developing commercially for clinical applications in cardiology, gastroenterology, oncology, and dermatology [3–6]. In cardiology, intravascular optical coherence tomography (IV-OCT) is a promising imaging technique to monitor many cardiovascular interventions and visualize cardiovascular disease [7–10]. The performance of IV-OCT is superior in resolution and scanning speed to intravascular ultrasound imaging systems [11], which has led to many investigations [12–18]. Standard IV-OCT acquires radial cross-sections and three-dimensional cylindrical volumes of a blood vessel by rotating and pulling back an intravascular fiber-optic imaging probe (i.e., optical fiber plus GRIN lens plus prism) to collect structural information about the tissue based on the optical backscattered light intensity. IV-OCT is analogous to intravascular ultrasound imaging, except reflections of near-infrared light are collected and detected by a CCD camera, rather than an ultrasound transducer. Systems have combined a standard IV-OCT catheter with other imaging modalities such as fluorescence, ultrasound, and photoacoustic imaging [19, 20].

The addition of contrast agents for IV-OCT imaging can potentially enable molecularly sensitive and site-specific cardiovascular imaging. Several different types of exogenous contrast agents have been investigated to improve the capabilities of detecting and localizing disease sites for diagnosis [21–24]. These molecularly sensitive OCT contrast agents function by modifying local optical properties such as absorption and scattering [25–28]. For example, plasmonic gold nanoparticles are relatively biocompatible and may provide not only imaging contrast via scattering but also photothermal therapy via absorption [27, 28].

A novel class of contrast agents are magnetically responsive particles that function as dynamic and molecularly-specific OCT contrast agents and include magnetic nanoparticles (MNPs) and magnetic microspheres (MSs) [23–30]. Magnetic MSs, due to their core-shell structure, are especially attractive since the relatively larger volume of the core can contain therapeutic drugs and the protein shell can be readily functionalized for site-specific targeting. Previous studies demonstrated that these MSs can also generate contrast in ultrasound imaging and MRI (negative–T2 contrast) [23–29]. The core can be loaded with hydrophobic drugs for targeted drug delivery applications [31] and/or lipophilic fluorescence dyes for fluorescence-based optical imaging [24–30].

Magnetomotive OCT (MM-OCT) is a functional extension of OCT which utilizes magnetically responsive exogenous particles such as MNPs and MSs [32–36]. Briefly, when these particles in tissue are modulated by an alternating magnetomotive force induced by an external magnetic field, the tissue will deform on the nanometer to micrometer scale due to the physical displacement and perturbation of the excited magnetic particles. The resulting tissue displacement can be detected by OCT based on intensity and/or phase changes in the optical signal. This will result in not only dynamic contrast enhancement but also molecularly-specific contrast enhancement for OCT because these particles can be functionalized to target a specific biomolecule or receptor. This MM-OCT concept is somewhat analogous to ultrasound elastography [37], and is also useful for characterizing the mechanical properties of tissue [38, 39].

In this study, we developed a metal-free catheter-based intravascular magnetomotive optical coherence tomography (IV-MM-OCT) system and demonstrated its performance by using RGD-functionalized magnetic MSs to target $\alpha_v\beta_3$ integrins that are overexpressed in diseased atherosclerotic rabbit aortas. These MSs were loaded with magnetic iron-oxide nanoparticles and further coated with polyethylene glycol (PEG) to extend circulation time of the MSs *in vivo*.

2. Experimental

2.1 Animal and magnetic microsphere preparation

The rabbits ($n = 7$; New Zealand white male rabbits; Myrtle's Rabbitry, Thompson's Station, TN) used in this study were divided into healthy ($n = 1$) and diseased groups ($n = 6$). In the diseased group, six rab-

bits, after a physiological adjustment period of one week on standard chow diet (Teklad 2031 Global High-Fiber Rabbit Diet; Harlan, Indianapolis, IN), were started on an atherogenic diet for 8–12 weeks [40, 41]. The one rabbit in the healthy group was fed a standard chow diet (Teklad; Harlan, Indianapolis, IN) for 8–12 weeks. Experiments were performed in compliance with an experimental protocol approved by the Institutional Animal Care and Use Committee at the University of Illinois at Urbana-Champaign.

The preparation method for making these microspheres has been described in our previous studies [23–30]. Briefly, the magnetic MSs are formed through the process of emulsification of vegetable oil and BSA protein aggregation due to the application of high intensity ultrasound sonication. The raw MSs were then coated with PEG_{5kDa} to extend the circulation time *in vivo* [42]. In our group, the MS fabrication parameters (data not shown) were previously investigated, including the length of the PEG chain and the labelling ratio between the BSA and the PEG peptides. The PEG_{5kDa}-coated MSs were then conjugated with cyclic RGD peptide on their shells to target the $\alpha_v\beta_3$ integrin. The resulting mean diameter of the MSs measured by a Coulter Counter (Multisizer 4, Beckman Coulter, Inc., Brea, CA) was 2.5 ± 1.28 μm, which was suitable for use as a blood-pool contrast agents, yet small enough to circulate through capillary beds.

2.2 In vivo microsphere injection and ex vivo IV-MM-OCT imaging

After approximately 8 weeks, healthy or diseased rabbits were first intravenously injected with manganese (2 mM, 1 mL) 5 minutes prior to the *in vivo* injection of MSs or PBS to activate the $\alpha_v\beta_3$ integrin binding sites on the early fatty streaks and atherosclerotic plaques [43]. The rabbits were then intravenously injected with one of the following three solutions: 1) PBS (1 mL), 2) non-targeted MS ($\sim10^9$ MSs/mL), and 3) targeted MSs ($\sim10^9$ MSs/mL). After 30 min of *in vivo* circulation time, rabbits were euthanized and their aortas were rapidly excised for *ex vivo* IV-MM-OCT imaging. Each aorta specimen was washed three times with fresh PBS to remove luminal fluid and blood clots before IV-MM-OCT imaging. A transparent plastic guide sheath (tube) was then inserted into each aorta specimen as it was held in a bath filled with $1\times$ PBS (~200 mL). The average length of each aorta segment was about 5 cm. After each aorta specimen was in place in the bath, a custom-built metal-free IV-OCT probe mounted on top of a translation stage (Figure 1) was then inserted through the plastic guide tube. A series of M-mode scans (Figure 3) was taken at regular in-

tervals over a 32 mm pull-back distance. The OCT catheter pullback rate (0.018 mm/sec) was matched to the OCT scan rate (2,795 Hz). Following each pull-back, each aorta specimen was rotated about 30 degrees around its long axis to acquire a minimum of three longitudinal OCT scans at different locations. When IV-MM-OCT imaging was completed, each aorta specimen was removed from the bath and cryo-preserved for frozen sectioning and haematoxylin and eosin (H&E) staining.

2.3 Histological Analysis

Pathological features of fatty streaks and plaques were identified visually on gross specimens, and histologically using H&E staining. The pathological features on H&E-stained aorta sections were confirmed by a blinded board-certified pathologist (Dr. Sandhya Sarwate) to identify atherosclerotic stage (healthy, early, and advanced atherosclerosis).

2.4 Statistical analysis

There were two different groups (diseased and healthy) and four different conditions in this study: 1) diseased rabbit injected with targeted MSs ($n = 3$; diseased-targeted MSs), 2) diseased rabbit (early stage atherosclerosis) injected with targeted MSs ($n = 2$; early stage-targeted MSs), 3) diseased rabbit injected with non-targeted MSs ($n = 1$; diseased-non-targeted MSs), and 4) healthy rabbit injected with PBS ($n = 1$; healthy-PBS). The statistical correlation between groups was investigated by analysis of variance (ANOVA; 95% confidence interval) statistics followed by pairwise comparisons with post hoc Bonferroni correction (R software ver. 2.15.0). All values were given as mean $\pm$ standard deviation of magnetomotive signal.

3. Results

Figure 1 shows a schematic diagram of the prototype IV-MM-OCT setup including a custom-built metal-free OCT catheter and a dual-coil magnetic solenoid configuration offering a long working distance (~6 cm). The light source of the IV-MM-OCT system was a superluminescent diode at 1310 nm, giving a measured axial resolution of 6 μm (full width half maximum). The working distance, transverse resolution, and diameter of the metal-free OCT catheter were 3 mm, 54 μm, and 1 mm, respectively. An external magnetic field modulated at 250 Hz was
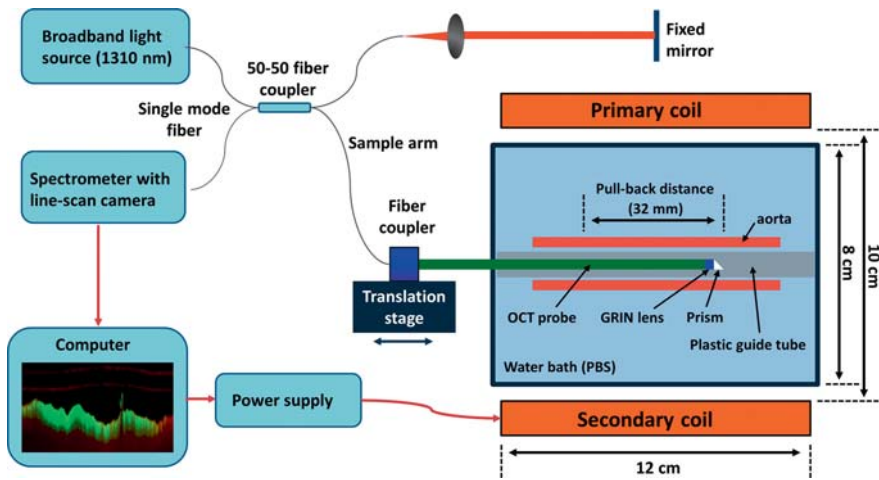
Figure 1 Schematic diagram of the IV-MM-OCT system for *ex vivo* imaging of rabbit aortas. A prototype metal-free intravascular OCT probe was used to avoid any interference with the applied alternating magnetic field. The axial and transverse resolutions (6 μm and 54 μm) are comparable to a standard intravascular OCT probe. The pull-back distance was 32 mm. The two coils were identical in size and magnetic field strength. The magnetic field gradient was 0.25 T/m.
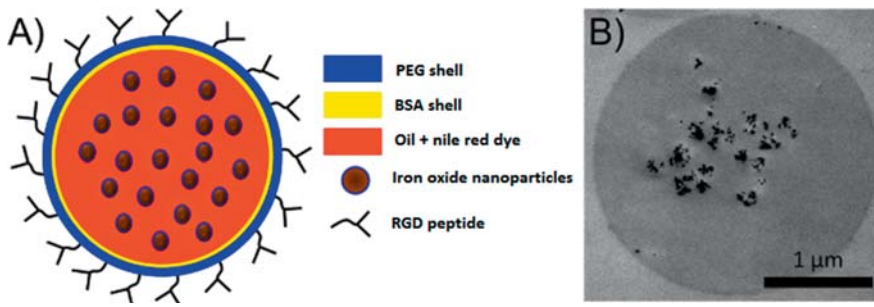

Figure 2 Magnetomotive microspheres as dynamic contrast agent. A conceptual drawing of the magnetic microsphere structure (**A**), and a transmission electron microscope (TEM) image of a single magnetic microsphere (**B**). The dark objects in the core of the microsphere are single and aggregated iron oxide nanoparticles.

generated by primary and secondary electromagnetic coils [34]. The magnetic field strengths at the surface of the primary coil and at a distance of 6 cm were 0.025 T and 0.01 T, respectively. The resulting magnetic field gradient was 0.25 T/m. This magnetic field gradient was sufficient to perturb the MSs on the aortic endothelium.

The MSs used for this study have a core-shell structure (Figure 2). Their core consists of vegetable oil and the shell is made of bovine serum albumin (BSA) protein. A variety of hydrophobic substances can be incorporated within the vegetable oil core such as iron oxide nanoparticles and fluorescent dyes. To target the $\alpha_v\beta_3$ integrin, PEG_{5kDa}-coated MSs were functionalized with cyclic arginyl-glycyl-aspartic acid (RGD) peptide on their shell. The targeted (with RGD) or non-targeted (without RGD) MSs were subjected to the external 250 Hz magnetic field generated by the primary and secondary electromagnetic coils.

A transparent plastic guide tube was inserted into each *ex vivo* aorta as it was held in a bath filled with PBS. Structural OCT data (composed of a series of adjacent M-mode scans; Figure 3) was then taken at regular intervals with a custom-built metal-free OCT catheter during a catheter pullback rate of 0.018 mm/sec over a pullback distance of 32 mm. At each step, M-mode images consisting of 512 A-lines were acquired at a A-scan rate of 2,795 Hz. Longitu-

dinal B-mode images (2048 A-lines) were then reconstructed by taking discrete Fourier transforms of the resampled M-mode images.

Figure 4A shows the healthy and diseased aorta specimens after the rabbits were on about 8 weeks of normal and high cholesterol diet, respectively.
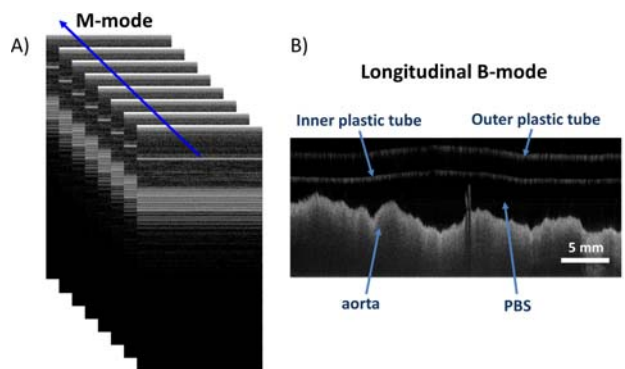

Figure 3 Imaging scheme for intravascular magnetomotive OCT. M-mode images (**A**) were acquired at each step during catheter pull back. Each M-mode image consisted of 512 A-lines. Approximately 46 cycles of the alternating magnetic field were recorded in each M-mode image. A complete catheter pull-back consisted of 2048 M-mode images. A longitudinal B-mode image (**B**) was subsequently generated by re-sampling A-lines along the blue line shown in (**A**).
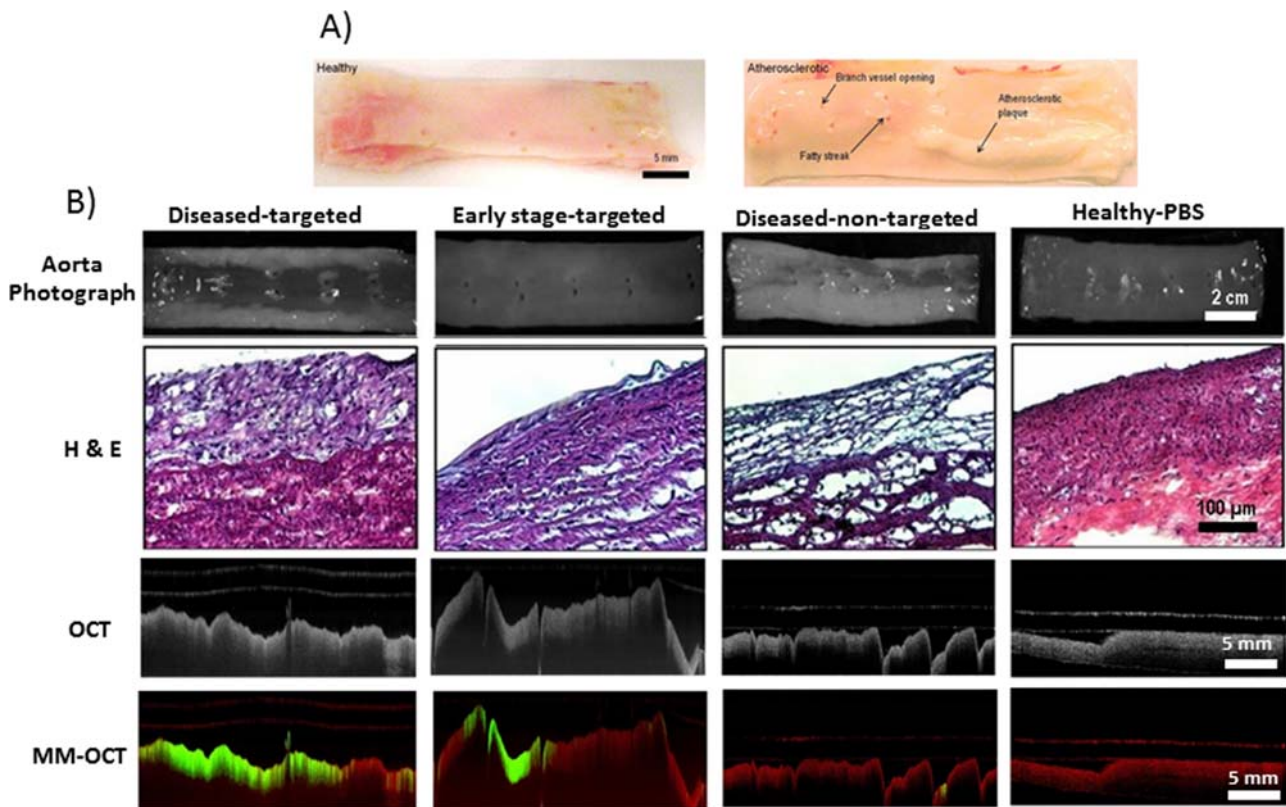
Figure 4 Rabbit aortas (**A**) after 8–12 weeks of normal and high-fat diet, along with representative images (**B**) of aorta specimens (row 1), H&E-stained tissue sections (row 2), OCT images (row 3), and IV-MM-OCT images (row 4; MM signal in green channel and structural OCT intensity in red channel). There were statistically significant differences in mean magnetomotive signal between the groups of diseased-targeted vs. diseased-non-targeted ($p < 0.01$), and diseased-targeted vs. healthy-PBS ($p < 0.01$).

Notably, the diseased group rabbit aortas revealed the presence of early-stage and advanced atherosclerotic plaques and fatty streaks around branch vessel openings. However, the aorta specimens from a healthy rabbit showed no visual indications of disease. Figure 4B shows representative images of aorta specimens (row 1), H&E-stained tissue sections (row 2), OCT images (row 3), and IV-MM-OCT images (row 4) generated by superimposing the MM signal (green channel) and the structural OCT intensity (red channel).

There were statistically significant differences (Figure 5; Table 1) in the MM signal between conditions: 1) the diseased-targeted MSs vs. the diseased-non-targeted MSs ($p < 0.01$) and 2) the diseased-targeted MSs vs. the healthy-PBS ($p < 0.01$). However, there was no statistically significant difference ($p > 0.06$) in the MM signal between the diseased-targeted MSs (2.08 ± 0.45 dB) and the early stage-targeted MSs (1.71 ± 0.18 dB). In addition, the mean MM-OCT signals in the diseased-non-targeted MSs and the healthy-PBS conditions are 1.23 ± 0.04 dB and 1.25 ± 0.05 dB, respectively. The hematoxylin and eosin (H&E; Figure 4B) stained aorta sections
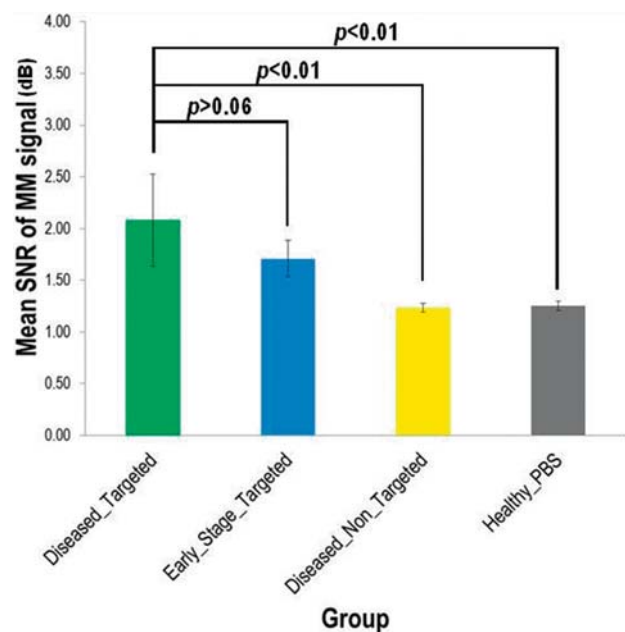

Figure 5 Statistical comparison of mean magnetomotive signal between groups.

Table 1 Measured magnetomotive signal.

Group	No. of scan locations	Mean (± SD) of MM-signal (dB)	p-value (between groups)
Diseased – Targeted MSs ($n = 3$)	11	2.08 ± 0.45[a]	
Early stage – Targeted MSs ($n = 2$)	10	1.71 ± 0.18[a]	> 0.06[b]
Diseased – Non-targeted MSs ($n = 1$)	5	1.23 ± 0.04[a]	< 0.01[c]
Healthy – PBS ($n = 1$)	3	1.25 ± 0.05[a]	< 0.01[d]

[a] Reported mean (± SD) values were obtained from the total number of MM-OCT scan locations within each group.
[b] Reported p-value was measured between the diseased-targeted MSs group and the early stage-targeted MSs group.
[c] Reported p-value was measured between the diseased-targeted MSs group and the diseased-non-targeted MSs group.
[d] Reported p-value was measured between the healthy group and the early stage-targeted MSs group.

corresponding to the IV-MM-OCT scan locations were in good agreement with the IV-MM-OCT image findings.

A low level of magnetomotive signal is seen in the MM-OCT images (Figure 4B) from the diseased-non-targeted MS group and the healthy-PBS group. This is due to the low level of non-specific binding of the non-targeted MSs, and the low level background noise of the OCT image. Additionally, MM signal appears in deeper layers of the tissue, even though the targeted MSs (O.D. ~3 μm) are not able to penetrate through the endothelium. These image artifacts are likely due to optical phase changes caused by the oscillating MSs at the superficial layer, impacting the optical signal from the deeper layers. This artifact may also be due to the chemical bonding (i.e., mechanical coupling) between the targeted MSs and the endothelium. The mechanical oscillations of the MSs caused by the external alternating magnetic field may be propagating through the surrounding medium (e.g., intima, media, and adventitia of a blood vessel), also resulting in optical phase changes in the OCT image. Because these dynamic agents are used primarily for localizing pathologic changes in the vascular endothelium, any depth-resolved characterization of lesions can be performed by examining the standard, structural IV-OCT data that would accompany the MM-OCT signal, and which has been demonstrated is numerous previous studies [23–30].

4. Discussion and conclusion

In this study, we have developed a prototype metal-free catheter-based IV-MM-OCT system using an external dual-coil electromagnet configuration, and successfully detected early stage fatty streaks and advanced atherosclerotic lesions using $\alpha_v\beta_3$ integrin-targeted magnetic MSs. The molecularly sensitive and dynamic contrast generated by the functionalized magnetic MSs can potentially improve the diagnostic capabilities of intravascular OCT. With the use of the external magnetic coils [44], and the fabrication of metal-free imaging catheters [45], this technique would be capable of leveraging the use of existing IV-OCT commercial systems. We note several limitations in this study, and establish future directions towards the end goal of developing a system capable of *in vivo* IV-MM-OCT imaging.

A number of improvements in the imaging catheter design and electromagnetic coil configurations are under investigation for future IV-MM-OCT imaging. In this study, we performed *in vivo* injection, circulation, and targeting of MSs, followed by IV-MM-OCT imaging of resected *ex vivo* aorta specimens because the outer diameter of our custom prototype metal-free OCT catheter (O.D. ~1 mm) was problematic for ready *in vivo* access to the rabbit aorta for IV-MM-OCT imaging of atherosclerotic changes. Future research will involve further reduction of catheter diameter and/or use of a larger animal model. Standard intravascular OCT acquires 3D volumetric data of a blood vessel by pulling back the OCT probe that is in constant rotation. In this study, our IV-MM-OCT system only performed longitudinal B-mode imaging in pull-back mode without radial scanning. In the future, we will incorporate our custom-built metal-free OCT catheter with a fibre optic rotary joint mounted on a translation stage allowing us to acquire full 3D images of the aorta. Although a rotating fibre catheter might increase the phase noise and introduce distortions, many of these effects can be corrected and compensated [46], suggesting that phase-resolved IV-MM-OCT should be feasible.

The experimental setup and phase-resolved processing makes the current study more sensitive to the induced displacements of the MSs in the direction of the beam axis. In future configurations, we envision using multiple dual coils at various angular positions that are activated in synchronization with the rotation of the probe. An array of these coils could conceivably be placed externally across the chest during intravascular imaging. Moreover, catheters with the magnetic coil incorporated within the catheter itself are also under investigation. In this

study, we used a relatively lower OCT A-scan rate (2,795 Hz) compared to a standard IV-OCT A-scan rate (~50 kHz), so that a sufficient number of magnetic field modulation cycles could be obtained at each spatial location. In future studies, faster scan speeds can be achieved by applying the modulating frequency during the pullback of the catheter (or during the acquisition of a rotational scan) and by satisfying the temporal and spatial oversampling requirements for magnetomotive imaging [32]. Moreover, acquisition of volumetric IV-MM-OCT data might also be feasible [47], where multiple rotational scans can be acquired per modulation cycle and the phase differences between these can be utilized to detect the magnetomotive response, allowing the utilization of the high scan rates available with the current swept source OCT systems. Alternatively higher modulating frequencies can also be used to enable faster imaging speeds. A higher modulation frequency can be achieved by lowering the electrical impedance of the coils and optimizing the driving power circuit.

The application of IV-MM-OCT for *in vivo* measurements will introduce several challenges, most notably physiological motions associated with breathing and heart rate. These artifacts can potentially be minimized either by synchronizing the data acquisition with these physiological motions or by bandpass filtering around the modulation frequency [33].

In summary, we have shown that early-stage fatty streaks and plaques were successfully detected with a prototype intravascular MM-OCT system in conjunction with $\alpha_v\beta_3$ integrin-targeted magnetic MSs. Future *in vivo* IV-MM-OCT imaging is possible and would require fabrication of metal-free imaging catheters capable of rotational scans and a modified electromagnetic coil that can be placed externally for large animal or human investigations.

Disclosures All authors declare that they have no conflict of interest except Stephen A. Boppart, who receives royalties from the Massachusetts Institute of Technology for patents related to optical coherence tomography.

Conference presentation Kim J. et al., *Development of an Intravascular Magnetomotive Optical Coherence Tomography System*, Optical Society of America, Biomedical Optics (BIOMED), Miami, Florida, April 26–30, 2014.

Author biographies Please see Supporting Information online.

References

[1] World Health Organization (WHO), Global status report on noncommunicable diseases 2010, Geneva (2011).

[2] J. Kotowski, G. Wollstein, L. S. Folio, H. Ishikawa, and J. S. Schuman, Ophthalmic Surg Lasers Imaging **42**(Suppl.), S6–S14 (2011).

[3] J. Coletta, N. Suzuki, B. R. Nascimento, H. G. Bezerra, N. Rosenthal, G. Guagliumi, A. M. Rollins, and M. A. Costa, Arq Bras Cardiol **94**, 250–254, (2010).

[4] T. S. Kirtane and M. S. Wagh, Gastroenterol Res Pract **2014**, 376367 (2014).

[5] F. T. Nguyen, A. M. Zysk, E. J. Chaney, J. G. Kotynek, U. J. Oliphant, F. J. Bellafiore, K. M. Rowland, P. A. Johnson, and S. A. Boppart, Cancer Res **69**, 8790–8796 (2009).

[6] L. Schmitz, U. Reinhold, E. Bierhoff, and T. Dirschka, J Dtsch Dermatol Ges **11**, 499–507 (2013).

[7] D. Huang, E. A. Swanson, C. P. Lin, J. S. Schuman, W. G. Stinson, W. Chang, M. R. Hee, T. Flotte, K. Gregory, C. A. Puliafito, and J. G. Fujimoto, Science **254**, 1178–1181 (1991).

[8] G. J. Tearney, S. Waxman, M. Shishkov, B. J. Vakoc, M. J. Suter, M. I. Freilich, A. E. Desjardins, W. Y. Oh, L. A. Bartlett, M. Rosenberg, and B. E. Bouma, JACC Cardiovasc Imaging **1**, 752–761 (2008).

[9] M. R. Jones, G. F. Attizzani, C. A. Given, 2nd, W. H. Brooks, M. A. Costa, and H. G. Bezerra, AJNR Am J Neuroradiol **33**, 1494–1501 (2012).

[10] M. U. Farooq, A. Khasnis, A. Majid, and M. Y. Kassab, Vasc Med **14**, 63–71 (2009).

[11] J. Kochman, A. Pietrasik, A. Rdzanak, J. Jakala, W. Zasada, A. Scibisz, L. Koltowski, K. Proniewska, E. Pociask, and J. Legutko, Kardiol Pol **72**, 534–540 (2014).

[12] G. J. Tearney, S. A. Boppart, B. E. Bouma, M. E. Brezinski, N. J. Weissman, J. F. Southern, and J. G. Fujimoto, Opt Lett **21**, 534–545 (1996).

[13] G. J. Tearney, M. E. Brezinski, B. E. Bouma, S. A. Boppart, C. Pitris, J. F. Southern, and J. G. Fujimoto, Science **276**, 2037–2039 (1997).

[14] J. A. Ayers, W. C. Tang, and Z. Chen, Proceedings of the IEEE Sensors **1**, 497–500 (2004).

[15] S. K. Nadkarni, B. E. Bouma, J. de Boer, and G. J. Tearney, Lasers Med Sci **24**, 439–445 (2009).

[16] M. J. Suter, S. K. Nadkarni, G. Weisz, A. Tanaka, F. A. Jaffer, B. E. Bouma, and G. J. Tearney, JACC Cardiovasc Imaging **4**, 1022–1039 (2011).

[17] H. Yoo, J. W. Kim, M. Shishkov, E. Namati, T. Morse, R. Shubochkin, J. R. McCarthy, V. Ntziachristos, B.

E. Bouma, F. A. Jaffer, and G. J. Tearney, Nat Med **17**, 1680–1684 (2011).

[18] Z. Wang, D. Chamie, H. G. Bezerra, H. Yamamoto, J. Kanovsky, D. L. Wilson, M. A. Costa, and A. M. Rollins, Biomed Opt Express **3**, 1413–1426 (2012).

[19] Y. Yang, X. Li, T. Wang, P. D. Kumavor, A. Aguirre, K. K. Shung, Q. Zhou, M. Sanders, M. Brewer, and Q. Zhu, Biomed Opt Express **2**, 2551–2561 (2011).

[20] S. Liang, A. Saidi, J. Jing, G. Liu, J. Li, J. Zhang, C. Sun, J. Narula, and Z. Chen, J Biomed Opt **17**, 070501 (2012).

[21] K. Chen, Y. Liu, G. Ameer, and V. Backman, J Biomed Opt **10**, 024005 (2005).

[22] J. K. Barton, J. B. Hoying, and C. J. Sullivan, Acad Radiol **9**(Suppl 1), S52–S55 (2002).

[23] T. M. Lee, A. L. Oldenburg, S. Sitafalwalla, D. L. Marks, W. Luo, F. J. Toublan, K. S. Suslick, and S. A. Boppart, Opt Lett **28**, 1546–1548 (2003).

[24] F. J. Toublan, S. A. Boppart, and K. S. Suslick, J Am Chem Soc **128**, 3472–3473 (2006).

[25] U. Morgner, W. Drexler, F. X. Kartner, X. D. Li, C. Pitris, E. P. Ippen, and J. G. Fujimoto, Opt Lett **25**, 111–113 (2000).

[26] C. Yang, L. E. McGuckin, J. D. Simon, M. A. Choma, B. E. Applegate, and J. A. Izatt, Opt Lett **29**, 2016–2018 (2004).

[27] T. S. Troutman, J. K. Barton, and M. Romanowski, Opt Lett **32**, 1438–1440 (2007).

[28] J. Xi, Y. Chen, and X. Li, Biomed Opt Express **4**, 842–851 (2013).

[29] R. John, F. T. Nguyen, K. J. Kolbeck, E. J. Chaney, M. Marjanovic, K. S. Suslick, and S. A. Boppart, Mol Imaging Biol **14**, 17–24 (2012).

[30] S. A. Boppart, A. L. Oldenburg, C. Xu, and D. L. Marks, J Biomed Opt **10**, 41208 (2005).

[31] O. Grinberg, M. Hayun, B. Sredni, and A. Gedanken, Ultrason Sonochem **14**, 661–666 (2007).

[32] A. L. Oldenburg, V. Crecea, S. A. Rinne, and S. A. Boppart, Opt Express **16**, 11525–11539, (2008).

[33] R. John, R. Rezaeipoor, S. G. Adie, E. J. Chaney, A. L. Oldenburg, M. Marjanovic, J. P. Haldar, B. P. Sutton, and S. A. Boppart, Proc Natl Acad Sci USA **107**, 8085–8090 (2010).

[34] J. Kim, A. Ahmad, and S. A. Boppart, Opt Express **21**, 7139–7147 (2013).

[35] J. Kim, A. Ahmad, M. Marjanovic, E. J. Chaney, J. Li, J. Rasio, Z. Hubler, D. Spillman, K. S. Suslick, and S. A. Boppart, Mol Imaging Biol **16**, 36–43 (2014).

[36] J. Kim, J. Oh, T. E. Milner, and J. S. Nelson, Nanotechnology **18**, 035504 (2007).

[37] K. W. Hollman, S. Y. Emelianov, J. H. Neiss, G. Jotyan, G. J. Spooner, T. Juhasz, R. M. Kurtz, and M. O'Donnell, Cornea **21**, 68–73 (2002).

[38] V. Crecea, A. L. Oldenburg, X. Liang, T. S. Ralston, and S. A. Boppart, Opt Express **17**, 23114–23122 (2009).

[39] A. Ahmad, J. Kim, N. A. Sobh, N. D. Shemonski, and S. A. Boppart, Biomed. Opt. Express **5**, 2349–2361, (2014).

[40] J. L. King, R. J. Miller, J. P. Blue, Jr., W. D. O'Brien, Jr., and J. W. Erdman, Jr., Nutr Res **29**, 343–349 (2009).

[41] B. W. Smith, D. G. Simpson, S. Sarwate, R. J. Miller, J. P. Blue, Jr., A. Haak, W. D. O'Brien, Jr., and J. W. Erdman, Jr., J Ultrasound Med **31**, 711–720 (2012).

[42] F. M. Veronese and G. Pasut, Drug Discovery Today **10**, 1451–1458 (2005).

[43] O. Dormond, L. Ponsonnet, M. Hasmim, A. Foletti, and C. Ruegg, Thromb Haemost **92**, 151–161 (2004).

[44] E. M. Wassermann and S. H. Lisanby, Clin. Neurophysiol **112**, 1367–1377 (2001).

[45] C. L. Petersen, E. I. McNamara, R. B. Lamport, M. Atlas, J. M. Schmitt, E. A. Swanson, and P. Magnin, US Patent 6891984 (2005).

[46] C. Sun, F. Nolte, K. H. Y. Cheng, B. Vuong, K. K. C. Lee, B. A. Standish, B. Courtney, T. R. Marotta, A. Mariampillai, and V. X. D. Yang, Biomed Opt Express **3**, 2600–2610 (2012).

[47] A. Ahmad, J. Kim, N. D. Shemonski, M. Marjanovic, and S. A. Boppart, J. Biomed Opt **19**, 126001 (2014).